IOPscience iopscience.iop.org

Home Search Collections Journals About Contact us My IOPscience

Lattice dynamics in copper indium diselenide by inelastic neutron scattering

This article has been downloaded from IOPscience. Please scroll down to see the full text article.

1999 J. Phys.: Condens. Matter 11 3987

(http://iopscience.iop.org/0953-8984/11/20/305)

View the table of contents for this issue, or go to the journal homepage for more

Download details:
IP Address: 171.66.16.214
The article was downloaded on 15/05/2010 at 11:35

Please note that terms and conditions apply.

J. Phys.: Condens. Matter **11** (1999) 3987–3995. Printed in the UK PII: S0953-8984(99)00148-4

Lattice dynamics in copper indium diselenide by inelastic neutron scattering

P Derollez†, R Fouret†, A Laamyem†, B Hennion‡ and J Gonzalez§

† Laboratoire de Dynamique et Structure des Matériaux Moléculaires, Université de Lille I, 59655 Villeneuve d'Ascq Cédex, France
‡ Laboratoire Léon Brillouin, CEA/Saclay, 91191 Gif sur Yvette, France
§ Centro de Estudios de Semiconductores, Facultad de Ciencias, Universidad de Los Andes, Merida 5101, Venezuela

Received 15 December 1998, in final form 17 March 1999

Abstract. The phonon dispersion curves along the [100] and [001] directions of $CuInSe_2$ have been measured by inelastic neutron scattering. The neutron measurements reveal the uncertainty of optical measurements because of the large absorption of this material. The lattice dynamics is analysed with a rigid ion model: Born–von Karman short range interactions associated with long range electrostatic forces. The calculated dispersion curves are in good agreement with the experiment. The atomic displacements associated with each vibrational mode are used to discuss the optical phonons. The obtained results provide a strong experimental basis from which we can validate the *ab initio* methods.

1. Introduction

The ternary semiconductors of the $A^IB^{III}C_2^{VI}$ family (where A = Cu, Ag; B = In, Ga, Al and C = Se, S, Te) adopt the tetragonal chalcopyrite structure (space group $I\bar{4}2d$) shown in figure 1. They can be considered as being derived from the zinc-blende structure by doubling the conventional unit cell along the c-axis. The replacement of the cationic sublattice by two different atomic species induces:

(i) a tetragonal distortion represented by the parameter $\eta = c/2a$ and
(ii) anion displacements to non-cubic positions characterized by the parameter $u = 0.25 + (d^2_{\mathrm{I-VI}} - d^2_{\mathrm{III-VI}})/a^2$.

Because of these structural (η, u) and chemical (A $\neq$ B) parameters, the chalcopyrite compounds exhibit a wide range of physical properties. Their dynamical study may be regarded as an extension of the work previously made on the blende-type materials. In this paper, we focus our attention on the lattice dynamics of $CuInSe_2$ (CIS) in order to obtain a better knowledge of the restoring forces.

CIS is a direct energy gap semiconductor ($E_g \sim 1$ eV at 300 K) which has attracted much attention in the past decades because it is known to be a promising semiconductor for the fabrication of high-efficiency thin-film solar cells due to its high absorption coefficient, suitable band gap and good chemical stability [1].

The lattice parameters at 300 K are $a = 5.782$ Å and $c = 11.620$ Å [2]. We notice that $\eta = 1.005$ characterizes a dilatation along the c-axis, which is not generally the case in

0953-8984/99/203987+09$19.50 © 1999 IOP Publishing Ltd

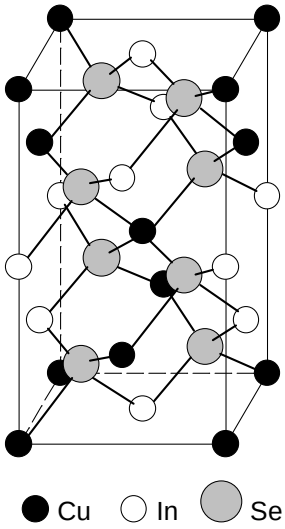

Figure 1. Chalcopyrite structure of $CuInSe_2$.

Table 1. Fractional coordinates of the atoms in the primitive cell.

Cu1	0	0	0
Cu2	1/2	0	−1/4
In1	0	−1/2	−1/4
In2	1/2	−1/2	0
Se1	−1/4	u	−1/8
Se2	$-u$	−1/4	1/8
Se3	u	1/4	1/8
Se4	1/4	$-u$	−1/8

I–III–VI_2 chalcopyrites [2]. u is found to be $u = 0.235$. The primitive cell includes eight atoms whose fractional coordinates are given in table 1.

The structural, optical and electrical properties of CIS have been investigated in detail by many authors [2–9]. Lattice vibrational studies by Raman scattering and infrared reflectivity have also been reported in the literature [10–16], but strong disparities are found on the determination of some vibrational frequencies. Acoustic phonon measurements by inelastic neutron scattering have yielded elastic stiffness constants and compressiblity [17]. The present paper reports a more complete determination of the phonon dispersion curves in the [100] and [001] directions, which has made possible a lattice dynamics analysis of CIS, using a rigid ion model.

2. Experimental results

A single crystal was grown by the horizontal Bridgman technique, with a volume of about 0.12 cm^3. Inelastic neutron scattering experiments have been carried out at room temperature and atmospheric pressure at the Orphée reactor at the Laboratory Léon Brillouin on the triple axis spectrometer 1T installed on a thermal source. The monochromator and the analyser were pyrolytic graphite in (002) reflection. The measurements have been performed at a constant k_F of 2.662 $Å^{-1}$ with a graphite filter placed after the sample to prevent higher order

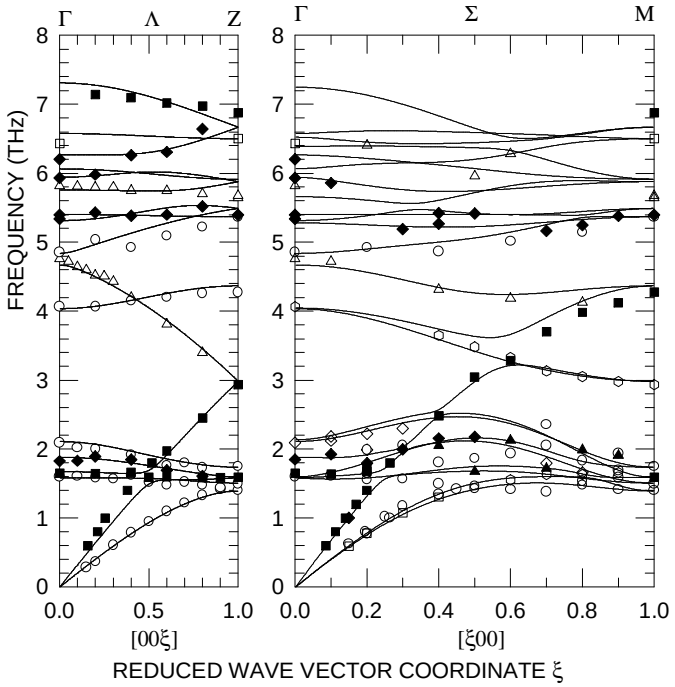

Figure 2. Dispersion curves of phonons along the [001] and [100] directions. The points correspond to the neutron measurements, the full line to the BvK model.

contamination. The horizontal collimations were 30′–40′–40′–40′ yielding an FWHM energy resolution of 0.2 THz for zero energy transfer.

In addition to the previously measured acoustic modes [17], optical phonon branches have been measured over the whole energy range in the [100] and [001] directions. As there are eight atoms in the primitive cell, 24 branches are expected in a general direction. In the [001] direction, degeneracies reduce this number to 17, the irreducible decomposition being $5\Lambda_1 + 5\Lambda_2 + 7\Lambda_3$, where the Λ_3 modes are doubly degenerated. Due to the small sample size and to its large neutron absorption, the signal was rather weak and we could not tighten the resolution as much as we would have desired. In order to get reasonable hints to optimize the intensity of a selected branch, we used a group-theoretical analysis and an estimate of the dynamical structure factor of the neutron scattering cross-section, with a rough Born–von Karman model. This was achieved with the Unisoft program package [18]. The collected data have been systematically corrected from instrumental resolutions and the resulting frequencies along [001] and [100] are reported in figure 2.

3. Discussion

The frequencies measured at the Γ-point are reported in table 2, together with results of IR and Raman measurements. Some disparities are observed. Some of them point out erroneous results, such as the E^3 mode determination by Syrbu *et al* [16], but there is also a systematic discrepancy between the neutron and Raman measurements. A possible explanation could reside in the very weak penetration of the laser beam in CIS during Raman measurements. Tanino *et al* [15] mention indeed a penetration depth of about 100 nm, leading to a higher

Table 2. Comparison of our neutron frequencies at the Γ-point with Raman and infrared results. The symbol * indicates an extrapolated value, the symbols [a] and [b] infrared reflectivity and Raman scattering measurements, respectively.

	[10]		[15] R		This work	
	IR[a]	[11–14]	300 K	[16]	Neutron	Calculated
Symmetry	R[b]	IR	100 K	IR	frequencies	frequencies
A_1			5.28		5.34	5.31
	5.58		5.34			
A_2^1					5.90	5.94
A_2^2					4.83	4.83
E^1	8.21/7.44	6.87/6.39	6.90/6.51	6.82/6.12	6.44	6.80/6.58
	8.24/7.55		6.99/6.51			
E^2				5.22/4.86	5.95	6.30/6.06
			6.90/6.81			
E^3	5.73/5.64	6.36/6.21	6.33	3.85/3.66	5.42	5.60/5.40
	5.73		6.48/6.33			
E^4	4.59/4.59	5.49/5.37		3.48/3.24	4.07	4.04/4.04
			5.64/5.64			
E^5	2.34/2.34			2.32/2.13	2.09	2.12/2.11
	2.34		2.34/2.34			
E^6		2.01/1.92	1.80/1.74	1.71/1.66	1.59	1.58/1.58
	1.83		1.80/1.83			
B_1^1					6.20	6.27
			6.87			
B_1^2					4.76	4.67
	4.74		5.37			
B_1^3					1.85	1.88
	3.51		2.01			
B_2^1	8.21/7.44	6.96/6.42	6.99/6.45	6.85/6.25	7.15*	7.31/6.52
			6.99/6.51			
B_2^2	5.88/5.64	5.79/5.43	5.94	5.07/4.89	5.82	5.76/5.28
	5.82		6.00/5.31			
B_2^3		1.95/1.92	2.13/2.10	2.36/2.11	1.65	1.67/1.59
	2.88		2.16/2.10			

sensitivity to surface effects (surface preparation, strain induced by polishing etc) and to an increase of the surface temperature by laser radiation. All these effects can broaden the measured phonon linewidth and shift the frequencies. Nevertheless, there is an overall agreement between the general distribution of modes and their assignment.

To analyse the experimental data, a Born–von Karman model (BvK) including short range and electrostatic forces was used. The term of the dynamical matrix corresponding to Coulomb forces was calculated following the Ewald summation method. The short range forces have been assumed to be central and their contribution to the dynamical matrix is then characterized by L and T: the longitudinal and transverse force constants. We have taken into account short range force constants up to 5 Å, which includes interactions between first- and second-neighbour ions. To avoid the multiplicity of adjustable parameters, the same values were used for equivalent pairs with slightly different distances, as can be seen in table 3. From the magnitude of the LO–TO splitting, Tanino *et al* [15] have determined the following effective charges: $Z_{Cu} = 0.475$, $Z_{In} = 1.255$ and $Z_{Se} = -0.865$. These values were kept fixed in the refinements since no significant improvement was obtained. We used about 50 measured frequencies: the zone centre values, the zone boundary values in the [100] and [001] directions

Table 3. Equilibrium distances and atomic force constants for the considered interactions.

Interaction	Shell radius (Å)	L (N m^{-1})	T (N m^{-1})
Cu1–Se1	2.46	54.8	−7.0
	4.77–4.84–4.87	−0.3	1.9
In1–Se1	2.56	120.7	−15.1
	4.72–4.79–4.82	5.3	0.5
Cu1–Cu2	4.10	7.0	0.6
Cu1–In1	4.10	0.2	−2.1
Cu1–In2	4.09	0.2	−2.1
In1–In2	4.10	−7.9	1.0
Se1–Se2	4.04	2.4	2.1
Se1–Se4	3.97	2.4	2.1
Se1–Se2	4.16	2.4	2.1
Se1–Se4	4.21	2.4	2.1

and some values measured at [0.5, 0, 0] and [0, 0, 0.5]. The refinement of the 16 force constants which were adjusted using the Unisoft program [18] linked to a least-squares fit routine yielded a reliability factor of 1.9%. The final values of the parameters are reported in table 3. The standard deviations for the force constants L and T of the preponderant Cu1–Se1 and In1–Se1 interactions are about 3%; the other parameters are less well defined (standard deviations less than 20%). The phonon dispersion curves calculated with the force constants of table 3 and the effective charges mentioned above are shown in figure 2. The fit to the experiment is excellent. The calculated atomic displacements for each vibrational mode are given in table 4. The complex conjugate eigenvectors of the doubly degenerated E modes are not mentioned. Because of the non-centrosymmetric structure of chalcopyrites, a mode can be both Raman and infrared active. However, the A_1 and B_1 modes concern out-of-phase motions giving zero electric dipole moment and hence are only Raman active. The A_2 modes consist of out-of-phase motions of the anions inducing a zero resultant dipole moment. The motions of the degenerated E modes have a finite resultant dipole moment perpendicular to the c-axis. The B_2 optic modes involve out of phase motions of the two anion pairs along the a- or b-axes and in-phase motions of all ions along the principal axis and hence give a finite dipole moment along that direction. Figure 3 shows the phonon density of states calculated from the force constants of table 3. We observe three frequency ranges in accordance with the dispersion curves of figure 2. The molar heat capacity at constant volume calculated from the density of states is shown in figure 4. The Debye temperature gives the deviations of the crystal from a Debye solid. Its value $\theta_D = 275$ K at high temperature can be compared to $\theta_D(\infty) = 207$ K calculated by Oshcherin [19] from empirical considerations based on the Lindemann criterion.

The valence force-field (VFF) model which constitutes a more realistic model in such tetrahedrally coordinated crystals was also used. The short-range interatomic forces are described through bond stretching and bond bending forces. For CIS, the VFF model leads to two stretching and five bending constants [20] whose meaning and final values are reported in table 5. The standard deviations of the α and β parameters are about 4% and 25%, respectively. This model yields a reliability factor of 7.9% and hence does not describe the results as well as the previous model. The stretching constant α_{Cu-Se} and α_{In-Se} values which give the general shape of the dispersion curves are close than those derived from the BvK model. The bending constants are much weaker and some of them appear to be negative, probably because coupling interactions, such bond stretching–angular rigidity, angular rigidity–angular rigidity contributions, have been neglected in our expression of the potential energy of deformation. The shell model which accounts for electronic polarization leads to a reliability factor slightly

Table 4. Calculated frequencies in THz and eigenvectors in Cartesian coordinates of all zone-centre phonons in $CuInSe_2$. The upper signs (+ or −) correspond to the displacement patterns for one Cu, one In and two Se ions while the lower signs to the displacement patterns for the remaining one Cu, one In and two Se ions in the primitive cell. The complex conjugate eigenvectors of the doubly degenerated E modes are not mentioned.

Modes	Calculated frequencies	Eigenvectors in Cartesian coordinates			
		Cu	In	Se	Se
A_1	5.31	(0, 0) (0, 0) (0, 0)	(0, 0) (0, 0) (0, 0)	(0, 0) (±0.50, 0) (0, 0)	(∓0.50, 0) (0, 0) (0, 0)
A_2^1	5.94	(0, 0) (0, 0) (0, 0)	(0, 0) (0, 0) (0, 0)	(∓0.39, 0) (0, 0) (0.50, 0)	(0, 0) (∓0.39, 0) (−0.50, 0)
A_2^2	4.83	(0, 0) (0, 0) (0, 0)	(0, 0) (0, 0) (0, 0)	(±0.50, 0) (0, 0) (0.39, 0)	(0, 0) (±0.50, 0) (−0.39, 0)
E^1	6.80/6.58	(−0.03, ±0.01) (∓0.01, −0.03) (0, 0)	(0.27, ∓0.37) (±0.37, 0.27) (0, 0)	(−0.42, 0) (0, 0.12) (±0.50, 0)	(0.12, 0) (0, −0.42) (0, ∓0.50)
E^2	6.30/6.06	(−0.07, ±0.24) (∓0.24, −0.07) (0, 0)	(−0.30, ∓0.18) (±0.18, −0.30) (0, 0)	(−0.07, 0) (0, 0.50) (∓0.16, 0)	(0.50, 0) (0, −0.07) (0, ±0.16)
E^3	5.60/5.40	(0.37, ±0.34) (∓0.34, 0.37) (0, 0)	(0.19, ±0.08) (∓0.08, 0.19) (0, 0)	(−0.41, 0) (0, −0.14) (∓0.33)	(−0.14, 0) (0, −0.41) (0, ±0.33)
E^4	4.04/4.04	(0.34, ∓0.37) (±0.36, 0.34) (0, 0)	(−0.19, ∓0.23) (±0.23, −0.19) (0, 0)	(−0.06, 0) (0, −0.01) (∓0.09, 0)	(−0.01, 0) (0, −0.06) (0, ±0.09)
E^5	2.12/2.11	(0.34, ±0.36) (∓0.36, 0.34) (0, 0)	(−0.30, ∓0.02) (±0.02, −0.30) (0, 0)	(0.21, 0) (0, −0.16) (±0.38, 0)	(−0.16, 0) (0, 0.21) (0, ∓0.38)
E^6	1.58/1.58	(−0.14, ±0.18) (∓0.18, −0.14) (0, 0)	(0.13, ∓0.58) (±0.58, 0.13) (0, 0)	(0.25, 0) (0, −0.28) (∓0.24, 0)	(−0.28, 0) (0, 0.25) (0, ±0.24)
E^7	0	(0.45, 0) (0, 0.45) (0, 0)	(0.60, 0) (0, 0.60) (0, 0)	(0.50, 0) (0, 0.50) (0, 0)	(0.50, 0) (0, 0.50) (0, 0)
B_1^1	6.27	(0, 0) (0, 0) (±0.28, 0)	(0, 0) (0, 0) (±0.39, 0)	(0, 0) (0, ±0.50) (0, 0)	(±0.50, 0) (0, 0) (0, 0)
B_1^2	4.67	(0, 0) (0, 0) (±0.71, 0)	(0, 0) (0, 0) (∓0.38, 0)	(0, 0) (∓0.04, 0) (0, 0)	(∓0.04, 0) (0, 0) (0, 0)
B_1^3	1.88	(0, 0) (0, 0) (±0.34, 0)	(0, 0) (0, 0) (±0.71, 0)	(0, 0) (∓0.37, 0) (0, 0)	(∓0.37, 0) (0, 0) (0, 0)
B_2^1	7.31/6.52	(0, 0) (0, 0) (−0.22, 0)	(0, 0) (0, 0) (−0.66, 0)	(∓0.30, 0) (0, 0) (0.50, 0)	(0, 0) (±0.30, 0) (0.50, 0)
B_2^2	5.76/5.28	(0, 0) (0, 0) (−0.55, 0)	(0, 0) (0, 0) (0.05, 0)	(±0.50, 0) (0, 0) (0.21, 0)	(0, 0) (∓0.50, 0) (0.21, 0)
B_2^3	1.67/1.59	(0, 0) (0, 0) (0.71, 0)	(0, 0) (0, 0) (−0.57, 0)	(±0.41, 0) (0, 0) (0.03, 0)	(0, 0) (∓0.41, 0) (0.03, 0)
B_2^4	0	(0, 0) (0, 0) (0.45, 0)	(0, 0) (0, 0) (0.60, 0)	(0, 0) (0, 0) (0, 0.50)	(0, 0) (0, 0) (0, 0.50)

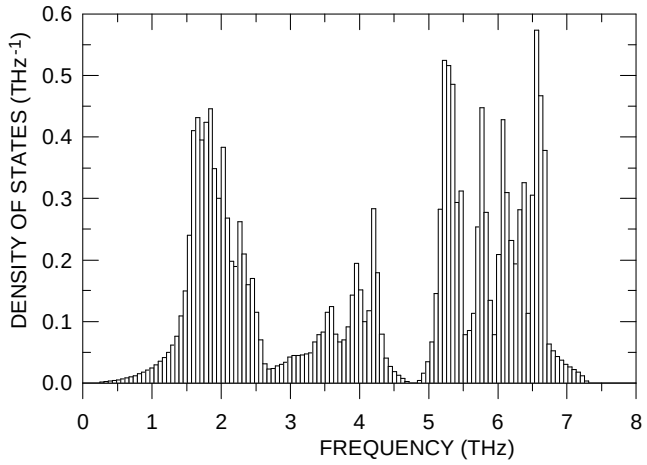

Figure 3. Phonon density of states of $CuInSe_2$ calculated from the BvK parameters given in table 3.

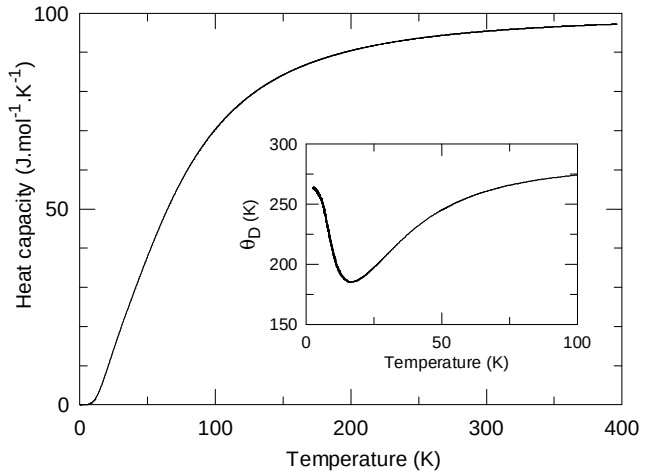

Figure 4. Molar heat capacity as a function of temperature calculated from the density of states (inset: variation of the Debye temperature).

better than those of the BvK model (reliability factor of 1.5%) but 36 adjustable parameters have been introduced in the refinements.

The predominant stretching constants $L_{\mathrm{Cu-Se}} = 54.8$ and $L_{\mathrm{In-Se}} = 120.7$ (in N m^{-1} unit) are close to the corresponding constants determined by Fouret *et al* [20] in $AgGaSe_2$: $L_{\mathrm{Ag-Se}} = 55.5$ and $L_{\mathrm{Ga-Se}} = 117.1$. On the other hand, the transverse force constants differ notably when passing from CIS ($T_{\mathrm{Cu-Se}} = -7.0$, $T_{\mathrm{In-Se}} = -15.1$) to $AgGaSe_2$ ($T_{\mathrm{Ag-Se}} = -9.7$, $T_{\mathrm{Ga-Se}} = -5.1$). The Raman and infrared inactive modes A_2 which involve motions of the anions only (see table 4) are at the following frequencies: 4.83 (4.83) and 5.94 (5.90) THz. These values can be compared to those determined in $AgGaSe_2$ by Fouret *et al* [20] by neutron measurements (4.68 and 6.25 THz) and calculated using a BvK model: (4.65 and 6.15 THz) and by Karki *et al* [21] from *ab initio* calculations (4.68 and 6.45 THz). As pointed out by Camassel *et al* [22], Fouret *et al* [20] and Karki *et al* [21], the optical phonon

Table 5. Parameters of the valence force-field model.

Type of bond	Bond constant	Final values (N m^{-1})
Cu–Se	α_1	59.8
In–Se	α_2	129.3
Se–Cu–Se	β_1	−1.3
Se–In–Se	β_1'	0.3
Cu–Se–In	β_2	−1.2
Cu–Se–Cu	β_3	4.1
In–Se–In	β_3'	−7.4

modes of $AgGaSe_2$ at the Γ-point are grouped into three frequency bands: namely a high frequency range 6.80–8.20 THz, an intermediate range 4.10–6.20 THz and a low frequency region 0.80–2.40 THz. This does not appear to be the case in CIS, where the optical phonons are only found in two main bands. The low frequency region 1.59–2.09 THz includes, at the Γ-point, the symmetry modes $E^6 + B_2^3 + B_1^3 + E^5$, as observed by Tanino *et al* [15]. These modes involve the displacements of all atoms (table 4) although the B_1^3 mode is dominated by the motion of the heavier indium atoms. The higher frequency range 4.07–7.15 THz for the remaining modes also involves all the atoms, except for the $A_1 + 2A_2$ modes which only involve the selenium atoms. The frequencies of the E^1 and B_2^1 modes which are dominated by the displacements of the In atoms are much smaller than those of $AgGaSe_2$. Therefore, the high frequency region tends to the intermediate range and a single phonon group is observed in CIS.

4. Conclusion

From the dynamical studies of chalcopyrite compounds, we find the following conclusions:

(i) A determination of the phonon branches owing to neutron measurements gives results which reveal, in this specific case, the uncertainty of optical measurements because of the large absorption of this material.

(ii) Despite its simplicity, the rigid ion model allows a general and realistic description of the dispersion curves of $CuInSe_2$ and $AgGaSe_2$ and can lead to more fruitful conclusions when comparing the force constants.

(iii) Finally, the obtained results provide a strong experimental basis from which we can validate the *ab initio* methods. Ackland *et al* [23] have discussed the treatment of errors in *ab initio* forces and showed the importance of correcting for errors in the case of $AgGaSe_2$. They have obtained a general description of the dispersion curves. Their calculated frequencies at the Γ-point are in good agreement with experiment. However, some discrepancies up to 1 THz can be observed at the Brillouin zone boundary, specially in the low frequency range.

Acknowledgments

The authors wish to thank Dr G Eckold who provided the program package Unisoft. One of us (JG) acknowledges the CEFI-PCP (France) and the CONICIT-Materials (Venezuela). This work was performed under the frame work of EEC Contract No CI1-CT94-0031. The Laboratoire de Dynamique et Structure des Matériaux Moléculaires is UPRESA 8024.

References

[1] Rocket A and Birkoure R W 1991 *J. Appl. Phys.* **70** R80
[2] Jaffe J E and Zunger A 1984 *Phys. Rev.* B **29** 1882
[3] Irie T, Endo S and Kimura S 1979 *Japan. J. Appl. Phys.* **18** 1303
[4] Wasim S M 1986 *Solar Cells* **16** 289
[5] Neumann H and Tomlinson R D 1990 *Solar Cells* **28** 301
[6] Rincon C, Gonzalez J and Sanchez Perez G 1981 *Phys. Status Solidi* b **108** K19
[7] Rincon C, Bellabarba C, Gonzalez J and Sanchez Perez G 1986 *Solar Cells* **16** 335
[8] Nakanishi H, Sawaya T, Endo S and Irie T 1993 *Japan. J. Appl. Phys.* **32** (Supplement 3) 200
[9] Nomura S, Matsushita H and Endo S 1996 *Cryst. Res. Technol.* **31** 813
[10] Gan J N, Tauc J, Lambrecht V G, Robbins Jr and M 1976 *Phys. Rev.* B **13** 3610
[11] Riede V, Sobotta H, Neumann H, Nguyen H X, Müller W and Kühn G 1978 *Solid State Commun.* **28** 449
[12] Neumann H, Sobotta H, Riede V, Schumann B and Kühn G 1983 *Cryst. Res. Technol.* **18** K90
[13] Neumann H 1986 *Solar Cells* **16** 399
[14] Neumann H, Tomlinson R D, Kissinger W and Avgerinos N 1983 *Phys. Status Solidi* b **118** K51
[15] Tanino H, Maeda T, Fujikake H, Nakanishi H, Endo S and Irie T 1992 *Phys. Rev.* B **45** 13 323
[16] Syrbu N N, Bogdanash M, Tezlevan V E and Mushcutariu I 1997 *Physica* B **229** 199
[17] Fouret R, Hennion B, Gonzalez J and Wasim S M 1993 *Phys. Rev.* B **47** 8269
[18] Eckold G *Unisoft: a Program Package for Lattice Dynamical Calculations: User Manual* 2nd revised edn Jül.Spez-366 (Institut für festkörperforshung der KFA, Jülich)
[19] Oshcherin B N 1976 *Phys. Status Solidi* a **35** K35
[20] Fouret R, Derollez P, Laamyem A, Hennion B and Gonzalez J 1997 *J. Phys.: Condens. Matter* **9** 6579
[21] Karki B B, Clark S J, Warren M C, Hsueh H C, Ackland G J and Crain J 1997 *J. Phys.: Condens. Matter* **9** 375
[22] Camassel J, Artus L and Pascual J 1990 *Phys. Rev.* B **41** 5717
[23] Ackland G J, Warren M C and Clark S J 1997 *J. Phys.: Condens. Matter* **9** 7861